Symmetry mode analysis of distorted polar/nonpolar structures in *A*-site ordered SmBaMn$_2$O$_6$ perovskite

J. Blasco [1,*] G. Subías [1] J. L. García Muñoz [2] F. Fauth [3] M. C. Sánchez[1] and J. García[1]

[1]*Instituto de Nanociencia y Materiales de Aragón (INMA), CSIC–Universidad de Zaragoza, 50009 Zaragoza, Spain*
and Departamento de Física de la Materia Condensada, Universidad de Zaragoza, C/ Pedro Cerbuna 12, 50009 Zaragoza, Spain
[2]*Institut de Ciència de Materials de Barcelona, ICMAB-CSIC, Campus UAB, 08193 Bellaterra, Spain*
[3]*CELLS-ALBA Synchrotron Light Source, 08290 Cerdanyola del Vallès, Barcelona, Spain*

We present a comprehensive structural study of the charge-orbital ordering and magnetic phase transitions observed in the *A*-site ordered SmBaMn$_2$O$_6$ perovskite combining synchrotron radiation x-ray powder diffraction and symmetry-adapted modes analysis. In SmBaMn$_2$O$_6$, successive phase transitions in charge, spin, and lattice degrees of freedom take place with decreasing temperature at $T_{CO1} \approx 380$ K, $T_{CO2} \approx 190$ K, and $T_N \approx 250$ K. The main difference between the two charge-ordered phases concerns the stacking sequence along the *c* axis, which is double for the high temperature charge-ordered phase and has led to controversy in the literature. We show that both charge-ordered phases are pseudosymmetric with respect to the ideal undistorted tetragonal structure of *A*-site ordered *R*BaMn$_2$O$_6$ perovskites and lead to two nonequivalent Mn sites. However, the charge segregation stabilizes at about $0.35e^-$ in the low temperature charge-ordered phase, clearly below the nominal separation of one charge unit between Mn^{3+} and Mn^{4+} and undergoes a prominent increase in the high temperature charge-ordered phase when warming above ≈ 250 K. The two Mn sites are anisotropic in both charge-ordered phases but the analysis of the active modes discloses that only the low temperature charge-ordered phase displays a Jahn-Teller-like distortion for one of the Mn sites. In addition, this low temperature charge-ordered phase has polar symmetry compatible with ferroelectricity along the *a* axis.

I. INTRODUCTION

SmBaMn$_2$O$_6$ (SBMO) is a half doped manganite with intriguing properties [1–3] and promising technological applications [4,5]. In this compound, competitive interactions between the different degrees of freedom (spin, charge, orbital) come into play together with the *A*-site ordering and the small size of Sm^{3+}, leading to stabilization of successive charge order (CO), orbital order (OO), and magnetic order [6]. The *A*-site ordering causes the MnO$_2$ sublattice to be sandwiched between the SmO and BaO sublattices of very different sizes inducing asymmetric distortions in the MnO$_6$ octahedron [7]. Finally, the small size of Sm^{3+} produces a structural strain that can be relieved with different tilts of the MnO$_6$ octahedra. The combination of *A*-site ordering and MnO$_6$ octahedral rotations can lift inversion symmetry through the trilinear coupling mechanism giving rise to a form of hybrid-improper ferroelectricity [8,9]. In such a case, two primary distortions are needed to reach a ferroelectric phase and intermediate phases may appear as occurs in related Aurivillius compounds [10]. All these factors make the crystallography of SBMO challenging.

The first studies on *A*-site ordered perovskites placed SBMO in a group characterized by two transitions: a CO transition at $T_{CO1} = 380$ K coupled to a metal-insulator transition and a magnetic transition around $T_N \approx 250$ K [11]. It is well known that metal-insulator transitions in manganites are associated with significant changes in the local structure of MnO$_6$ octahedra which are regular and distorted in the metallic and insulating phases, respectively [12]. Moreover, the magnetic order is considered antiferromagnetic (AFM) of CE-type according to isostructural compounds and T_N is placed in a peak of the magnetization as a function of the temperature [11]. The magnetic ordering could not be verified by neutron diffraction due to the strong absorption cross section of Sm atoms. However, the finding of $(h/4, k/4, l)_T$ superstructure reflections in transmission electron microscopy (TEM) measurements supports the occurrence of a lattice with periodicity $2\sqrt{2}\mathbf{a}_T \times \sqrt{2}\mathbf{a}_T \times \mathbf{c}_T$ (T subscript refers to the ideal *P*4/*mmm* tetragonal structure for *A*-site ordered perovskites) as expected for a CO phase with a CE-type magnetic ordering [11,13]. This type of magnetic ordering consists of ferromagnetic (FM) zigzag chains in the *ab* plane that are coupled AFM to each other and along the *c* axis [14]. In the CO phase there are two nonequivalent Mn sites ascribed to Mn^{3+} and Mn^{4+} and the former site displays a Jahn-Teller-like distortion attributed to an OO of e_g orbitals [15]. When comparing the properties of the compounds without cationic order (Sm$_{1/2}$Ba$_{1/2}$MnO$_3$) and with *A*-site ordering (SBMO),

*Corresponding author: Javier Blasco Instituto de Nanociencia y Materiales de Aragón, Departamento de Física de la Materia Condensada, CSIC–Universidad de Zaragoza, C/ Pedro Cerbuna 12, 50009 Zaragoza, Spain, jbc@unizar.es

it is observed that this order reinforces the AFM interactions of the Mn moments and the formation of a CO phase because $Sm_{1/2}Ba_{1/2}MnO_3$ exhibits neither CO nor AFM order but a spin-glass phase at low temperature [13,16–18].

A subsequent study of the CO phase at room temperature using electron diffraction revealed two types of superlattice reflections, $(h/4, k/4, l)_T$ and $(h/2, k/2, l/2)_T$, which implied that the lattice parameters for the CO phase were $2\sqrt{2}\mathbf{a}_T \times \sqrt{2}\mathbf{a}_T \times 2\mathbf{c}_T$ [19]. The doubling of the c axis with respect to the parent tetragonal cell was explained by a change of the OO pattern along the c axis in such a way that every two layers of MnO_6 octahedra, the position of the Mn^{3+} and Mn^{4+} sites were exchanged giving rise to the so-called stacking sequence AABB [19,20]. Furthermore, low temperature measurements of neutron diffraction and x-ray diffraction patterns on $TbBaMn_2O_6$ and SBMO, respectively, found that $(h/2, k/2, l/2)_T$ reflections had vanished below T_N [20]. This reveals a structural transition at $T_{CO2} \approx 190\,K$ and a lattice with periodicity $2\sqrt{2}\mathbf{a}_T \times \sqrt{2}\mathbf{a}_T \times \mathbf{c}_T$ for the low temperature CO (LT-CO) phase. Both CO phases are thought to have uniform OO and the change in the modulation along the c axis between these phases is attributed to a rearrangement of the OO stacking patterns which could be ABAB or AAAA, among several possibilities in the LT-CO [20,21]. A further survey of the resonant x-ray scattering reflections $(5/4, 5/4, 0)_T$ and $(3/2, 1/2, 1/2)_T$ at the Mn K edge confirms the occurrence of two different CO phases in SBMO and the transformation of the stacking pattern at T_{CO2}. The proposed stacking sequences are AABB and ABAB for the high temperature CO (HT-CO) and LT-CO phases, respectively [22]. However, a resonant diffraction work [23] at the Mn $L_{2,3}$ edge of the $(1/4, 1/4, 0)_T$ reflection discloses an increase of the integrated intensity of this reflection at T_{CO2} that can only be accounted for by an AAAA-type stacking of the OO. Moreover, this work has concluded a $(x^2 - z^2)/(y^2 - z^2)$-type OO in contrast to single-layered manganites.

Subsequently, studies on single crystals were carried out using the convergent-beam electron diffraction (CBED) technique [24]. Based on the systematic extinctions found in the CBED patterns, the space group (SG) *Pnam* (No. 62, standard setting *Pnma*) was found for the HT-CO phase. The patterns also revealed $2mm$ point symmetry for the LT-CO phase and the $P2_1am$ SG was proposed. According to this assignation, the CBED technique supports the change of the stacking sequence from AABB to AAAA in agreement with García-Fernández *et al.* [23]. One of the most important conclusions of this study is that SBMO adopts a polar crystal structure at the ground state. Based on this result, *ab initio* density-functional theory (DFT) calculations were performed and ferroelectricity was predicted in SBMO [2]. The dipoles are oriented along the a axis and the main polar displacement comes from shifts of the apical oxygens in the MnO_6 octahedra. If the polar structure of SBMO is confirmed, it would clearly show how the combination of laminar A-site and rocksalt B-site orderings in the perovskite cell stabilizes noncentrosymmetric structures through the trilinear coupling mechanism [9,25].

A recent study [26] of single-crystal x-ray diffraction analyzes the diffraction patterns at 300 and 150 K using the

SGs determined by the CBED technique. In both models there are two nonequivalent Mn sites and the results are evaluated as a composition of two modes: Q2 (Jahn-Teller) and Q3 (breathing). A checkerboard distribution of the two Mn sites is deduced for both phases. The structural refinement yields large charge segregation in the HT-CO phase at 300 K (about 80% of the nominal value) that has decreased significantly in the LT-CO phase. The noncentrosymmetric structure is confirmed for the LT-CO phase, thought in this refinement the main polar contribution arises from shifts of the basal oxygens in the MnO_6 octahedra [26]. With this structural information new DFT calculations were performed in addition to group-theory methods in order to explore competitive phases and the origin of the polar state [3]. The polar structure is analyzed in basis to four types of distortions belonging to four irreducible representations of the parent tetragonal structure (*P4/mmm*): SM2 (stripe distortion), M5− (tilt), M4+ (breathing) and GM5− (polar distortion). The simultaneous action of all of these distortions gives rise to a hybrid-improper mechanism that produces the polar ground state of SBMO [3]. Another interesting result was the finding of competitive phases whose stability can be modified by epitaxial strain, which opens the possibility of growing metastable phases in epitaxial films for electronic applications [3].

In most previous studies, it had been settled that T_{CO2} was below T_N, the Néel temperature matching a local maximum on the $M(T)$ curve close to 250 K [11,20,22,23]. The change in the stacking sequence of the OO above T_{CO2} was attributed to ferromagnetic correlations due to double exchange coupling that competes with the CO distortion. This competition was considered responsible for altering the modulation along the c axis [23]. This view has been challenged by magnetization measurements made on single crystals where the local maximum in the $M(T)$ curves is vanished [1,27]. The $M(T)$ curves display steps at the CO transition temperatures, and a further kink at 175 K suggests that T_N in these crystals is actually below T_{CO2}. Then the AFM ordering would develop in the polar phase [27]. Amazingly, magnetic measurements on the crushed single crystals recovered the peak centered around 250 K, suggesting that the FM correlations depend on the grain size [27].

Hence, both crystallographic and magnetic properties of SBMO are not settled yet. For this purpose, we have carried out a comprehensive structural study of SBMO using synchrotron radiation x-ray powder diffraction (SRXRD). An advantage of this technique is that complications due to twinning, domain formation, multiple scattering, and self-absorption are strongly minimized. It also allows a detailed mapping of structural properties as a function of temperature. We have taken full advantage of the analysis method in terms of symmetry-adapted modes in order to identify the distortions related to the CO phase transitions. Our study reveals specific structural features for each of the CO transitions and a surprising temperature dependence of the charge segregation between nonequivalent Mn sites with a sharp increase above T_N. Our study also reveals that all Mn sites are anisotropic in both CO phases but a Jahn-Teller-like distortion (expected from an OO) is only significant in the polar LT-CO phase and the most important ferroelectric contribution along the a axis is observed in an apical oxygen atom.

II. EXPERIMENT

Single crystals of $SmBaMn_2O_6$ were grown using the floating zone method from polycrystalline precursors. Stoichiometric amounts of dried Sm_2O_3, $BaCO_3$, and Mn_2O_3 were mixed, ground, and heated at $1000\,°C$ overnight. The resulting powder is reground, pressed into pellets, and sintered at $1250\,°C$ in a gas flow of H_2/Ar mixture (2% H_2) saturated in water vapor to achieve a reductive atmosphere ($P_{O2} \approx 10^{-11}$). This is required to prevent the formation of $BaMnO_3$ impurity [28]. Thus, the pellets are reground, pressed into rods, and sintered at $1375\,°C$ for 24 h in the same atmosphere. The rods were mounted in a homemade floating zone furnace with two semielliptical mirrors [29]. The growth was performed in the same reductive atmosphere with an overpressure of 2 bars. The seed and feed bars with diameters of 3.5 mm rotated in opposite directions at 20 rpm with a growth speed of 6 mm/h. After this step, the material is oxygen deficient, $SmBaMn_2O_{5+\delta}$ with $\delta \approx 0.1$. The next step consists of a topotactic oxidation by heating the boules at $400\,°C$–$450\,°C$ in an oxygen current flow for 24 h yielding the stoichiometric $SmBaMn_2O_6$ compounds. Some parts of the boules were ground and analyzed by powder x-ray diffraction.

Rietveld analysis of the x-ray patterns was performed using the FULLPROF package program [30] with symmetry mode analysis. The input file with the basis modes was obtained from the AMPLIMODES program [31] from the Bilbao Crystallographic server. The AMPLIMODES/SYMMODES and ISODISTORT programs [32] were used to explore the different distorted structures of the SBMO compound. The schematic illustrations of the crystal structures were obtained with the VESTA program [33].

The chemical composition of the powders was also tested using wavelength dispersive x-ray fluorescence spectrometry (Advant'XP+ model from Thermo Fisher) and the Sm:Ba:Mn stoichiometry agreed with the expected values within experimental error (1%).

Synchrotron radiation x-ray diffraction powder (SRXRD) patterns were measured at the MSPD beam line [34] of the Alba synchrotron (Cerdanyola del Vallès, Spain) using a high throughput position-sensitive detector MYTHEN compatible with a high photon flux to detect minor superstructure peaks. The samples were loaded in a borosilicate glass capillary (diameter of 0.5 mm) and kept spinning during data acquisition. A short wavelength, $\lambda = 0.4128\,Å$, was selected to reduce absorption. The value of λ was calibrated using a NIST standard silicon. We have performed two types of measurements; standard patterns to refine unit cell parameters were collected in heating and cooling ramps between 100 and 440 K. The rate was $0.5\,K\,min^{-1}$ and the total acquisition time was 6 min. With this procedure, we collected a pattern every 3 K on average. Secondly, SRXRD patterns with high statistics were measured at three selected temperatures (100, 330, and 440 K) with a total acquisition time of 30 min/pattern to perform a full structural characterization.

Magnetic measurements were carried out with a commercial Quantum Design (SQUID) magnetometer. The dc magnetization was measured between 5 and 400 K with an external field of 1 kOe.
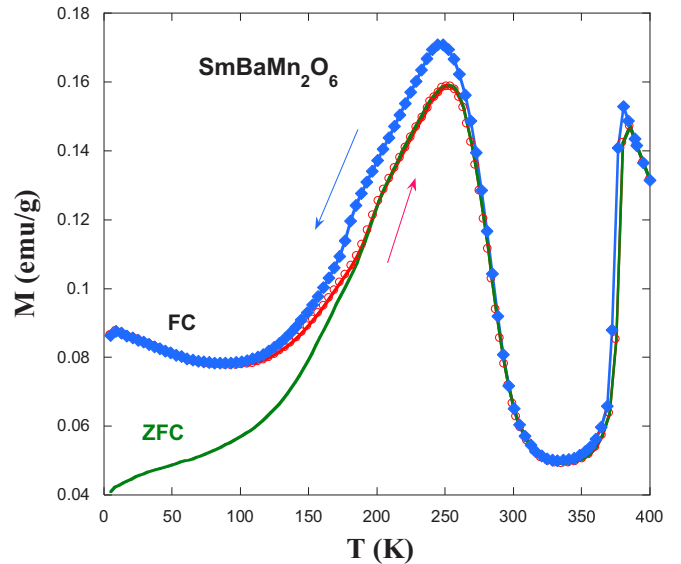
FIG. 1. Temperature dependence of the magnetization for $SmBaMn_2O_6$ in zero field cooling (ZFC) and field cooling (FC) conditions. FC measurements were performed in cooling and warming runs as indicated by the arrows.

III. RESULTS AND DISCUSSION

A. Magnetic properties and crystal structure of the high temperature phase

Figure 1 shows the temperature dependence of the magnetization for a crushed boule of $SmBaMn_2O_6$ between 5 and 440 K. Overall, the $M(T)$ curve agrees with those reported in previous studies [19,22,23]. The magnetization displays an abrupt drop at $T_{CO1} = 380$ K. We also see the maximum at around 250 K that was identified as T_N in preliminary studies [19,22,23]. Some features ascribed to T_{CO2} are more difficult to see in this measurement but a downturn point is seen around 200 K. The magnetization was measured in zero field cooled (ZFC) and field cooled (FC) conditions under an external field of 1 kOe. The ZFC and FC curves clearly show magnetic irreversibility suggesting the presence of competitive magnetic interactions. ZFC and FC branches begin to separate at 190 K, the expected temperature for T_{CO2}. The FC measurements performed in heating and cooling runs show hysteresis extending around 100 K in agreement with a previous study [23].

According to the magnetic properties shown in Fig. 1, we have selected three points to acquire SRXRD patterns with high statistics representative of the three different phases. The selected temperatures are 440 K (well above T_{CO1}), 330 K (in the flat area of the $M(T)$ curve below T_{CO1}), and 100 K (below T_{CO2} and T_N). Above T_{CO1}, different types of unit cells have been reported [19,24,26]. Our SRXRD pattern at 440 K can be indexed in a C-centered orthorhombic unit cell that agrees with Ref. [26]. This cell can be considered as a distorted cell of the parent tetragonal lattice with lattice vectors $(2, 0, 0)_T$, $(0, 2, 0)_T$, and $(0, 0, 1)_T$; i.e., the a and b axes are doubled in the orthorhombic cell and the SG *Cmmm* is adopted. According to the modes formalism [35], this orthorhombic phase can be described as a superposition of distortion modes corresponding to the irreducible
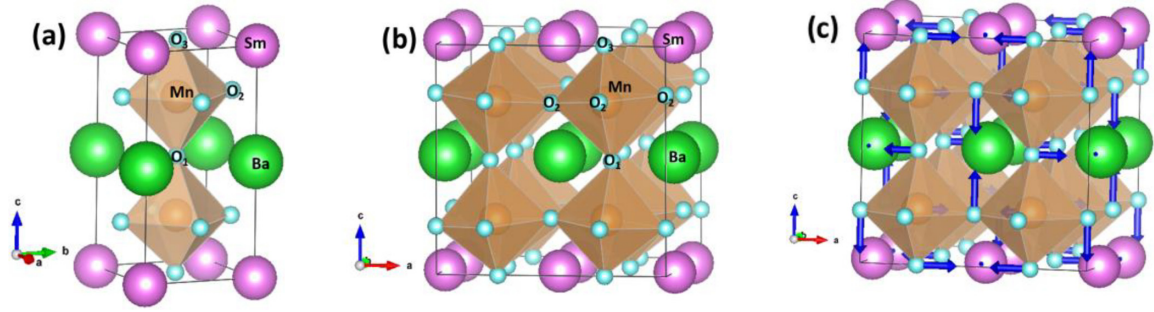
FIG. 2. Crystal structure of (a) the ideal undistorted tetragonal structure of SmBaMn$_2$O$_6$ with space group *P*4/*mmm* and (b) the orthorhombic structure at 440 K with space group *Cmmm*. (c) Detail of the atom displacements associated to the irrep M5− showing the rotation of the MnO$_6$ octahedra.

representations (irreps) of the undistorted tetragonal cell with symmetry *P*4/*mmm* and isostructural to the high temperature phase of related perovskites [36]. Nine distortion modes corresponding to three different irreps are permitted in the distortion from the *P*4/*mmm* cell into the *Cmmm* one. They are labeled as GM1+(2), GM2+(1), and M5−(6). The capital letters refer to the associated *k*-vector in the first Brillouin zone of the primitive tetragonal cell and the numbers in parentheses indicate the number of permitted individual modes for each irrep. Figure 2 shows the undistorted tetragonal cell and the orthorhombic one. Apical oxygens in MnO$_6$ octahedra are labeled as O1 (close to Ba atoms) and O3 (neighbor to Sm ones) whereas O2 atoms stand for basal oxygens. The two modes of the irrep GM1+ involve symmetric shifts of Mn and O2 layers along the *c* axis preserving the symmetry plane at $z = 1/2$. The mode of GM2+ implies a twisting distortion of the basal oxygens. The structural refinements reveal that the modes of both irreps are secondary with global amplitudes of 0.09(1) and 0.05(1) Å for GM1+ and GM2+, respectively. The primary contribution in this distorted structure corresponds to the modes of the irrep M5− with a global amplitude of 0.48(1) Å. Considering the individual modes of this irrep, the greatest contribution is observed by the displacement of oxygen atoms that can be seen as an antiphase rotation of the MnO$_6$ octahedron around the *b* axis as can be seen in Fig. 2(c). This rotation corresponds to the one-tilt system $a^0b^-c^0$ in Glazer's notation [37]. The oxygen shifts are not coupled and, in fact, the displacement of O1 is smaller than that of O3 due to the restrictions produced by the large size of the Ba^{2+} cation and therefore the MnO$_6$ octahedron is

no longer regular. Our refinement suggests that the driving force for this distorted structure is the strain produced by the small size of Sm^{3+} that is relieved by cooperative tilts of MnO$_6$ octahedra. In fact, the *Cmmm* SG was predicted for the above-mentioned one-tilt system by previous symmetry analysis on *A*-site ordered perovskites with MnO$_6$ rotations [38]. This structure was recently found in the NdBaMn$_2$O$_6$ phase diagram between 290 and 340 K [36]. The replacement of Nd by Sm stabilized this structure in a higher temperature range. The refined structural parameters are summarized in Table I and the experimental and calculated patterns can be found in the Supplemental Material [39] (Fig. S1) together with pictures of the displacements produced by several modes of the three irreps (Fig. S2).

B. Crystal structure of the nonpolar charge-order state: HT-CO

Below 380 K, there are strong changes of the unit cell parameters and the appearance of weak superstructure peaks as seen in Fig. 3. On the one hand, huge differences are observed in the splitting of the main peaks that no longer agree with the *Cmmm* crystal structure. More interesting is the temperature dependence of these superstructure peaks. The pattern collected at 330 K shows two types of superstructure peaks that can be indexed as $(h/4, k/4, l)_T$ and $(h/2, k/2, l/2)_T$. Both kinds of peaks are weak at this temperature, especially the latter. Only the $(h/4, k/4, l)_T$ peaks, whose intensity have increased, are observed in the pattern measured at 100 K while the $(h/2, k/2, l/2)_T$ peaks have vanished. This temperature dependence of the superstructure peaks agrees with previous

TABLE I. Structural parameters of SmBaMn$_2$O$_6$ obtained from the Rietveld analysis at 440 K.

	Atom	Pos.	x	Y	Z	B_{iso} (Å^2)
SG: *Cmmm*						
$a = 7.77629(2)$ Å	Sm	4*i*	0	0.7437(1)	0	0.85(1)
$b = 7.83221(2)$ Å	Ba	4*j*	0	0.7481(2)	$\frac{1}{2}$	0.67(1)
$c = 7.71776(2)$ Å	Mn	8*o*	0.2498(2)	0	0.2500(1)	0.45(7)
$V = 470.053(2)$ Å^3	O1	4*h*	0.2386(11)	0	$\frac{1}{2}$	0.6(1)
$R_p(\%) = 2.9$	O2$_1$	4*k*	0	0	0.7922(9)	0.8(1)
$R_{wp}(\%) = 4.3$	O2$_2$	4*l*	0	$\frac{1}{2}$	0.7517(9)	1.4(1)
$R_{Bragg}(\%) = 1.6$	O2$_3$	8*m*	$\frac{1}{4}$	$\frac{1}{4}$	0.2239(6)	1.1(1)
$\chi^2 = 4.75$	O3	4*g*	0.2805(9)	0	0	1.0(1)
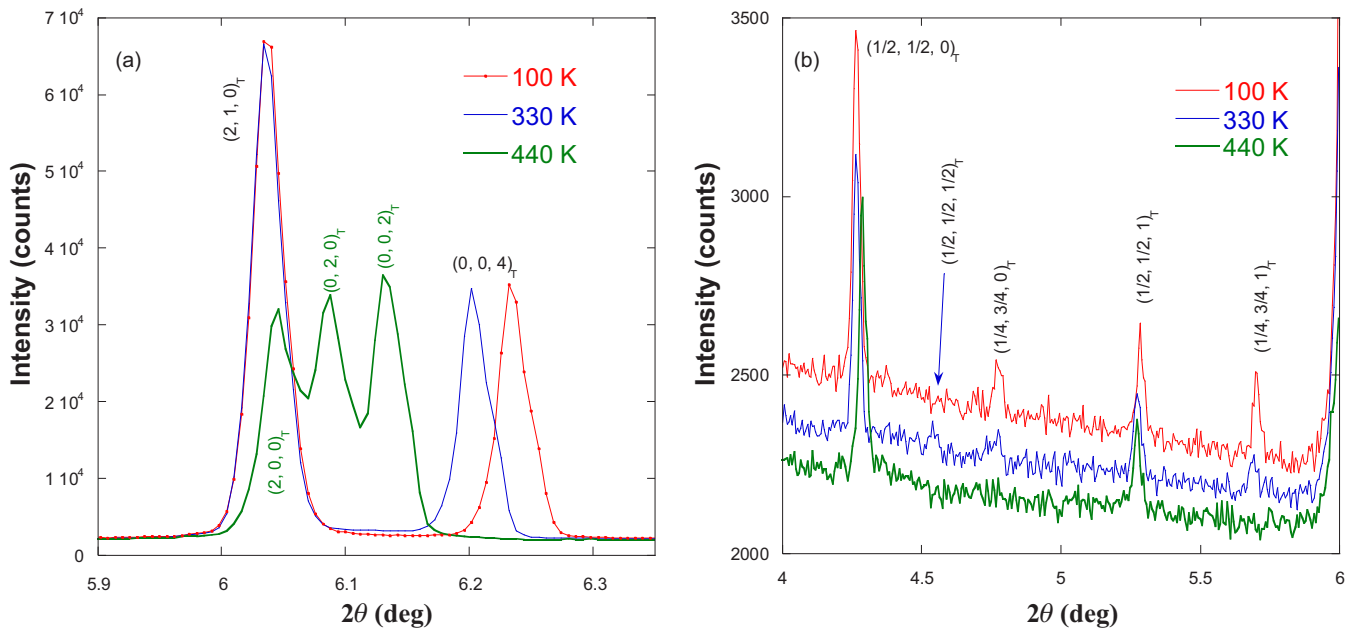
FIG. 3. Details of the SRXRD patterns showing (a) the changes of the splitting in the main diffraction peaks indicating a unit cell change, and (b) the occurrence of different superstructure peaks at different temperatures. The subscript T indicates that indexation of the peaks is related to the parent tetragonal cell.

reports [22–24,26]. Therefore, the pattern of SBMO at 330 K can be indexed with an orthorhombic cell with the following lattice parameters with respect to the parent tetragonal cell: $2\sqrt{2}\mathbf{a}_T \times \sqrt{2}\mathbf{a}_T \times 2\mathbf{c}_T$.

According to the CBED results [24], the SG for HT-CO is *Pnam* (No. 62, standard setting *Pnma*). We have used the ISODISTORT program [32] to explore possible distortions of the parent tetragonal structure that leads to this orthorhombic cell. We have found six possibilities (listed in the Supplemental Material [39], Table S1) but only two of them agree with the CBED study, which concludes that the planes *n*, *a*, and *m* are perpendicular to the *a*, *b*, and *c* axes, respectively [24]. The main difference between these two solutions concerns the point symmetry of the *A* atoms and apical oxygens that are related to the origin shift of the low symmetry cell in the basis of the parent tetragonal cell. In the first possible distorted structure, the origin shift is $(-1, -\frac{1}{2}, \frac{1}{2})$ and the Sm and O3 atoms in the tetragonal cell split into two orbits in the orthorhombic one and both orbits are located at Wyckoff position 4*c* with point symmetry *m*. However, Ba and O1 atoms have a single site in the orthorhombic cell, placed at the general Wyckoff position 8*d* with point symmetry 1. In the second possibility, the origin shift is $(-1, -\frac{1}{2}, 0)$ and these positions are interchanged. There are two nonequivalent sites for Ba and O1 atoms at the 4*c* sites whereas there is a single site for Sm and O3 atoms at the 8*d* position. In both cases, the tetragonal Mn site is split in two nonequivalent sites at the general position of the orthorhombic cell while the basal oxygen splits into four orbits with the same point symmetry 1. We have performed structural refinements using both models, obtaining accurate fits of the experimental results. However, the results and agreement factors are more congruent with the first model (for instance, compare Table III and Table S2 in the Supplemental Material [39] with the corresponding

discussion). It is worth noting that this structure is similar to the one selected by Ref. [26]. Table II shows the refined global amplitudes of each irrep for the *Pnam* phase at 330 K and Table III summarizes the resulting structural parameters using this model. The *Pnam* structure decomposes into 32 distortion modes that correspond to seven irreps of the *P4/mmm* structure. For the sake of comparison, we have performed a mode decomposition of the structural parameters reported by Sagayama *et al.* [26]. For this purpose we have used the AMPLIMODES program [31] from the Bilbao Crystallographic server and the results are also summarized in Table II. As can be seen, both refinements identify the same primary modes as belonging to the irrep M5− followed by the distortions ascribed to the irreps SM2 and S2. The rest of the modes are secondary and the contribution of the two modes from irrep A1+ is negligible. In view of Table II, the main difference between both studies concerns the global amplitude of SM2 modes. This difference could be related to differences in the studied specimens, the measurement temperature, and the different diffraction technique as Sagayama *et al.* carried out a single-crystal x-ray study refining anisotropic temperature factors for all atoms.

The schematic representation of the global atomic shifts for each irrep can be seen in the Supplemental Material [39] (Fig. S4). The Mn-O sublattice basically determines the magnetic and electrical properties of this compound. For this reason, we are going to focus on the distortions observed in the *Pnam* structure that affect those sublattices. First, regarding the global amplitudes in Table II, the most pronounced distortion is the tilt $a^-a^-c^0$ of the MnO6 octahedra that transforms according to irrep M5−. Secondly, the distortion modes corresponding to the irrep SM2 are responsible for the appearance of $(h/4, k/4, l)_T$ peaks. These modes include a set of atomic displacements that make the environments of the

TABLE II. Summary of the decomposition into symmetry-adapted modes of *P4/mmm* parent structure of the *Pnam* structure of SBMO reported in this work and in Ref. [26] at 300 K. The affected atoms and the corresponding isotropy subgroups ascribed to each irrep are included.

k-Vector	Irrep	Direction	Dim.	Atoms	Isotropy subgroup	Amplitude (Å)	
						This work	Sagayama *et al.* [26]
(0,0,0)	GM1+	(*a*)	2	Mn, O2	*P4/mmm*	0.145(18)	0.12
(1/4,1/4,0)	SM2	(*a*,0,0,−*a*)	8	All	*Pcma*	0.75(6)	0.395
(1/2,1/2,0)	M5−	(0,−*a*)	6	All	*Pmam*	1.00(4)	1.15
(1/2,1/2,1/2)	A1+	(*a*)	2	Ba, O2	*I4/mmm*	0.05(17)	0.04
(1/2,1/2,1/2)	A4+	(*a*)	3	Mn, O1, O2	*I4/mmm*	0.19(12)	0.34
(0,0,1/2)	Z5−	(0,−*a*)	5	Sm, Mn, O2, O3	*Bmmb*	0.29(13)	0.20
(1/4,1/4,1/2)	S2	(*a*,0,0,*a*)	6	Sm, Mn, O2, O3	*Bmab*	0.55(7)	0.505

two nonequivalent Mn sites different. With regard to the basal oxygens, it is of interest that each pair of atoms experiences the action of different distortions. Thus, the combination of three individual modes produces the shift of two basal oxygens in the *ab* plane whereas a fourth twisting mode leads to the displacement of the other two oxygens along the *c* axis in opposite directions. The following modes in importance correspond to irreps S2, Z5−, and A4+. They are responsible for the doubling of the tetragonal *c* axis because the distortions change their sign every two layers along *c* (see the Supplemental Material [39], Fig. S4). The main atomic shifts occur in the oxygen sublattice. In this way, (i) the distortion ascribed to the irrep A4+ comprises a displacement of the $O2_i$ ($i = 1$–4) and O3 atoms along the *a* axis but in opposite directions for layers $z = 1$–2 and $z = 3$–4. (ii) On the other hand, the oxygen displacements associated to the irrep Z5− are a breathinglike distortion of the O1 and $O2_i$ atoms favoring a CO between the two different MnO_6 octahedra. (iii) Finally, the S2 modes acting on the basal oxygens can be seen as complementary to the SM2 ones as they act over pairs of these oxygens. In the Supplemental Material [39] (Fig. S6) we show some combinations of both types of modes and the effects they could have on the formation of an OO.

The above-mentioned complex set of cooperative atomic shifts gives rise to the structure represented in Fig. 4. There are two types of MnO_6 octahedra whose distribution in the *ab* plane is exchanged every two layers along the *c* axis in agreement with the stacking sequence AABB. In the following we address the possible presence of CO and OO, separately. Our refinements yield two different MnO_6 octahedra with the bond lengths indicated in Table IV. This allows us to distinguish an expanded $Mn^{3+\delta}O_6$ and a compressed $Mn^{4-\delta}O_6$ octahedron with $\delta \approx 0.33$ using the bond valence sum (BVS) method [40]. Thus, the charge disproportionation between the two Mn sites is $\Delta q = 1$–$2\delta \approx 0.35\,e^-$. Δq is lower than the one reported in Ref. [26] at $T = 300$ K but this difference can be associated with small variances in the composition of both specimens. In this way, the greater amplitude of the SM2 modes observed in our sample (compare the data in Table II) suggests that the $(h/4, k/4, l)_T$ superstructure peaks are more intense in our sample. Moreover, the BVS calculations for the Mn atoms in the *Cmmm* phase give a valence of 3.49(1) in the present sample while the value reported in Ref. [26] is 3.35. This difference may be related to small changes in the oxygen content so the BVS value deduced for the Mn valence of our specimen agrees better with the theoretical oxygen stoichiometry.

Finally, the distortions observed in both MnO_6 octahedra are hard to conciliate with an OO of e_g $(x^2 - z^2)/(y^2 - z^2)$ orbitals alternately arranged at the $Mn^{3+\delta}$ sites. Instead, there is an even mixture of two types of distorted oxygen quadrilaterals in the *ab* plane. The $Mn^{4-\delta}$ has three short Mn-O2

TABLE III. Structural parameters of $SmBaMn_2O_6$ obtained from the Rietveld analysis at 330 K.

	Atom	Pos.	*X*	*Y*	*Z*	B_{iso} (Å^2)
SG: *Pnam*	Sm1	4*c*	0.8712(5)	0.2508(7)	$\frac{3}{4}$	0.76(9)
	Sm2	4*c*	0.1295(5)	0.7435(7)	$\frac{3}{4}$	0.52(9)
$a = 11.09311(3)$ Å	Ba	8*d*	0.8742(1)	0.2521(6)	0.0000(5)	0.56(2)
$b = 5.54385(2)$ Å	Mn1	8*d*	0.1260(8)	0.2421(9)	0.8717(5)	0.36(9)
$c = 15.26167(3)$ Å	Mn2	8*d*	0.3760(8)	0.7446(9)	0.8735(5)	0.32(10)
$V = 938.571(5)$ Å^3	O1	8*d*	0.1187(12)	0.226(3)	−0.004(2)	0.3(1)
	$O2_1$	8*d*	0.0070(13)	−0.005(2)	0.8521(11)	1.1(1)
$R_p(\%) = 3.9$	$O2_2$	8*d*	0.7545(13)	0.518(3)	0.8663(10)	1.1(1)
$R_{wp}(\%) = 5.6$	$O2_3$	8*d*	0.0055(13)	0.494(2)	0.8581(11)	1.1(1)
$R_{Bragg}(\%) = 1.75$	$O2_4$	8*d*	0.7513(13)	0.020(3)	0.8769(10)	1.1(1)
$\chi^2 = 5.1$	$O3_1$	4*c*	0.1477(13)	0.250(6)	$\frac{3}{4}$	0.9(2)
	$O3_2$	4*c*	0.3561(13)	−0.196(6)	$\frac{3}{4}$	0.9(2)
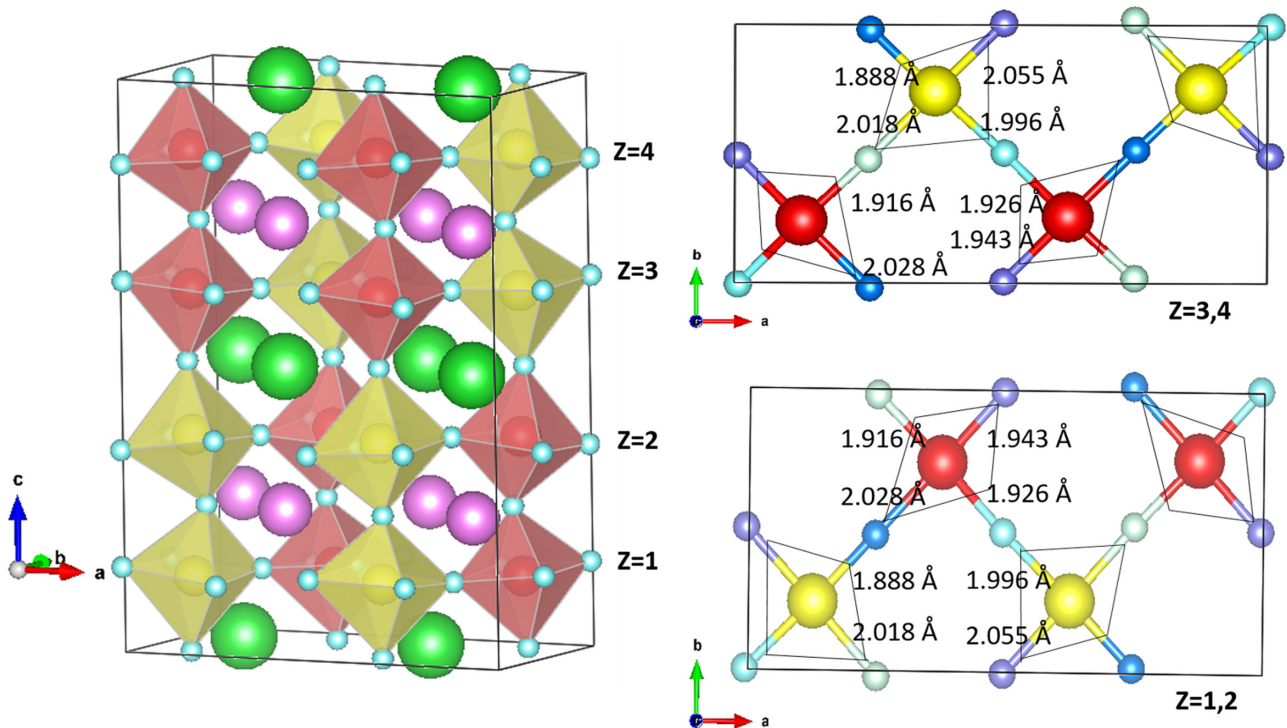
FIG. 4. (Left) Crystal structure of SmBaMn$_2$O$_6$ at 330 K (*Pnam*), corresponding to the HT-CO phase. (Right) Top view of the Mn-O layers at the indicated *z* values. The quadrilaterals drawn represent, in an exaggerated way, the geometry for the base of the MnO$_6$ octahedra.

distances and one long (kite shape) whereas the opposite distribution of bond lengths is observed for Mn$^{3+\delta}$. The top view of Fig. 4 illustrates the different coexisting geometric shapes defined by the Mn-O bond lengths. This figure shows that both types of MnO$_6$ octahedra are asymmetric and can give rise to resonant x-ray scattering.

C. Crystal structure of the polar charge-order state: LT-CO

As mentioned in the previous section, $(h/2, k/2, l/2)_\mathrm{T}$ peaks are not present in the SBMO pattern at 100 K. Therefore, this pattern can be indexed with an orthorhombic cell with $2\sqrt{2}\mathbf{a}_\mathrm{T} \times \sqrt{2}\mathbf{a}_\mathrm{T} \times \mathbf{c}_\mathrm{T}$ lattice parameters; i.e., the c axis is no longer doubled with respect to the parent tetragonal structure. According to CBED measurements [24], the SG for LT-CO is $P2_1am$ (No. 26, standard setting $Pmc2_1$). Exploring the possible distortions of the undistorted tetragonal phase using ISODISTORT [32], we have only found three possibilities and only one of them agrees with the CBED results presenting the following: screw axis perpendicular to the long a axis, n glide plane perpendicular to the short b axis, and m plane perpendicular to the c axis (see Table S3 in the Supplemental Material [39]).

The mentioned $P2_1am$ structure decomposes into 34 distortion modes comprised in six irreps of the parent tetragonal structure. The distorted structure has two nonequivalent sites for Mn, Sm, Ba, O1, and O3 atoms while O2 atoms split into four orbits. Table V shows the refined global amplitudes for each irrep and for the sake of comparison, we show in the same table the mode decomposition obtained for the structure reported in Ref. [26]. The refined Rietveld profile at 100 K is shown in Fig. S7 [39]. The crystal structure of the LT-CO

phase is displayed in Fig. 5 and the structural parameters are summarized in Table VI. Both refinements agree in the identification of the primary modes of the distorted structure that belong to the irreps M5− and SM2 with similar global amplitude although the latter has special importance here as will be discussed later. Contributions from GM5−, M4+, and GM1+ are secondary and the distortion arising from M1+ is negligible.

The main difference between both studies concerns the global distortion from the polar irrep GM5−. As our specimen was measured at a lower temperature (100 K), this might be related to an increase of the polar distortion with decreasing temperature.

A symmetry analysis of the $P2_1am$ phase was earlier reported and was applied to the Landau free energy expansion [3]. We review here the main symmetry-adapted modes of each irrep. The schematic representation of the distortions is shown in the Supplemental Material [39] (Fig. S8). Again, (i) the main distortion transforms as M5− (see Table V) and consists of a tilting of MnO$_6$ octahedra following the two-tilt system $a^-a^-c^0$. (ii) A symmetric breathing distortion of the basal oxygens corresponding to the irrep M4+ leads to a checkerboard arrangement of compressed and expanded MnO$_6$ octahedra in the *ab* plane. This distortion is coupled to a shift of the Mn atoms along the c axis, alternating in opposite directions along the three pseudocubic axes (therefore, inverted for compressed and expanded octahedra in the same plane). (iii) The largest number of individual modes corresponds to the irrep SM2. Note that there are remarkable differences from the SM2 modes observed in the HT-CO phase. Comparing this irrep in Tables II (HT-CO) and V (LT-CO) one can see that the distortions are applied along different

TABLE IV. Comparison of the bond lengths for the CO phases refined in this work to the ones reported in Ref. [26]. The expanded MnO_6 corresponds to $Mn^{3+\delta}$ while the compressed one matches $Mn^{4-\delta}$.

	Sagayama *et al.* [26]	This work
T (K)	300	330
Expanded MnO_6		
Mn-O1 $\times 1$ (Å)	1.967	1.995(31)
Mn-O2 $\times 1$ (Å)	2.105	2.050(14)
Mn-O2 $\times 1$ (Å)	2.086	2.019(17)
Mn-O2 $\times 1$ (Å)	2.002	1.996(14)
Mn-O2 $\times 1$ (Å)	1.927	1.891(17)
Mn-O3 $\times 1$ (Å)	1.892	1.926(9)
Valence (BVS)	3.18	3.29(7)
Compressed MnO_6		
Mn-O1 $\times 1$ (Å)	1.921	1.901(31)
Mn-O2 $\times 1$ (Å)	1.986	2.025(17)
Mn-O2 $\times 1$ (Å)	1.904	1.948(14)
Mn-O2 $\times 1$ (Å)	1.909	1.926(14)
Mn-O2 $\times 1$ (Å)	1.842	1.915(17)
Mn-O3 $\times 1$ (Å)	1.887	1.873(8)
Valence (BVS)	3.97	3.73(8)
T (K)	150	100
Expanded MnO_6		
Mn-O1 $\times 1$ (Å)	1.923	1.969(5)
Mn-O2 $\times 1$ (Å)	2.123	2.129(18)
Mn-O2 $\times 1$ (Å)	2.091	2.078(18)
Mn-O2 $\times 1$ (Å)	1.937	1.922(18)
Mn-O2 $\times 1$ (Å)	1.928	1.890(18)
Mn-O3 $\times 1$ (Å)	1.891	1.896(7)
Valence (BVS)	3.38	3.33(6)
Compressed MnO_6		
Mn-O1 $\times 1$ (Å)	1.941	1.914(4)
Mn-O2 $\times 1$ (Å)	1.988	2.008(17)
Mn-O2 $\times 1$ (Å)	1.943	1.978(17)
Mn-O2 $\times 1$ (Å)	1.889	1.894(17)
Mn-O2 $\times 1$ (Å)	1.879	1.883(17)
Mn-O3 $\times 1$ (Å)	1.895	1.894(4)
Valence (BVS)	3.89	3.76(6)

directions of the order parameter. In contrast to HT-CO, now the SM2 modes act on the four basal oxygens cooperatively (not only on half of them). Focusing on these oxygens, the individual modes allow rotation, asymmetric stretching, scissoring, and twisting distortions that act differently in the two types of MnO_6 octahedra enhancing their differences and giving rise to ordered distortions parallel to the *b* axis. This is why some authors have named the SM2 modes "stripe" distortions [3]. Its associated isotropy subgroup coincides with the final symmetry of the phase ($P2_1am$) and is compatible with electrical polarization along the *a* axis. (iv) However, the distortions that break the center of symmetry and can lead to electrical polarization are within the irrep GM5−. The distortions transforming like this irrep are composed of displacements along the *a* axis for the atoms that break the inversion center (Fig. S8) [39]. Given the polar character of this CO structure, we have fixed the distortion of Mn to zero as reference. Our refinements yield negligible polar shift for O1 atoms and a minor displacement of Sm, Ba, and O2 atoms in

the same direction as O3 atoms. It is noteworthy that the most important polar contribution arises from the apical oxygens as predicted from theoretical calculations [2] but it is centered in the shift of the O3 atoms, close to the small Sm^{3+} cation while the apical oxygen O1 close to the big Ba^{2+} cations is not displaced. Spontaneous polarization (P_S) was calculated using the equation

$$P_S = \sum_i (m_i \Delta x_i Q_i)/V,$$

where m_i is the site multiplicity, Δx_i is the atomic displacement along the *a* axis from the corresponding position in the nonpolar structure (i.e., amplitudes of GM5− modes set to zero), Q_i is the ionic charge of the *i*th constituent ion, and V is the unit cell volume [41]. The polar atomic displacements yield a value of $P_s = 1.35 \,\mu C\,cm^{-2}$. This value is a little lower than the theoretical predictions ($\approx 5\,\mu C\,cm^{-2}$) [2].

Alongside the polar nature of the $P2_1am$ crystal structure (Fig. 5 and Table VI), it is also important to highlight that the two MnO_6 octahedra exhibit substantial differences. The combination of the above-mentioned distortions leads to a Jahn-Teller-like distorted MnO_6 octahedron with the elongated axes indicated by a double arrow in the top view of the crystal structure [see Fig. 5(b)]. This distortion is located at the expanded MnO_6 octahedron ($Mn^{3+\delta}$) and changes its orientation 90° between two neighboring $Mn^{3+\delta}$ sites along the *a* axis while remaining unchanged along the *b* axis. The compressed MnO_6 octahedron ($Mn^{4-\delta}$) exhibits a trapezoid-based shape as indicated in the same figure, whose orientation between neighboring $Mn^{4-\delta}$ also changes along the same *a* axis. It is worth noting that this trapezoid-based shape is also found in the polar phases of $PrBaMn_2O_6$ and $NdBaMn_2O_6$ compounds with a single Mn site [36]. In the ground state of SBMO, there are two nonequivalent Mn sites with anisotropic environments that should be taken into account to properly describe the electronic anisotropy in the *ab* plane. Table IV summarizes the refined bond lengths for both MnO_6 units compared to the ones reported in Ref. [26]. Overall, the agreement is reasonable bearing in mind the small differences between both specimens indicated in the previous section. In contrast to the La, Pr, Nd compounds (with a single octahedral site), charge disproportionation occurs between the two nonequivalent Mn sites. In our refinement, it reaches a value of $\Delta q \approx 0.35\,e^-$, similar to the one reported by Sagayama *et al.* [26] for this phase and similar to the charge difference found in the HT-CO phase in this work. Moreover, this charge disproportionation between the two nonequivalent Mn atoms aligns well with that observed in other manganites with similar transitions and charge separation below the nominal one charge unit [42–44].

D. Temperature dependence of the structural properties

Figure 6(a) shows the evolution of the lattice parameters as a function of the temperature obtained under cooling and warming conditions. Two transitions are clearly noticeable. We have compared the equivalent axes referred to the ones of the high temperature *Cmmm* phase in this figure. The HT-CO develops at T_{CO1} and there is an expansion of the *ab* plane, especially strong for the *a* axis, while

TABLE V. Summary of the mode decomposition (with respect to $P4/mmm$) of the $P2_1am$ structure for SBMO reported in this work (100 K) and in Ref. [26] (150 K). The affected atoms and the corresponding isotropy subgroups ascribed to each irrep are included.

						Amplitude (Å)	
						This work	Sagayama *et al.* [26]
k-Vector	Irrep	Direction	Dim.	Atoms	Isotropy subgroup	100 K	150 K
(0,0,0)	GM1+	(a)	2	Mn, O2	$P4/mmm$	0.07(1)	0.13
(0,0,0)	GM5−	(a, a)	7	all	$C2mm$	0.25(4)	0.08
(1/2,1/2,0)	M1+	(a)	1	O2	$P4/mmm$	0.00(4)	0.03
(1/2,1/2,0)	M4+	(a)	2	Mn, O2	$P4/mmm$	0.15(5)	0.19
(1/2,1/2,0)	M5−	$(0,-a)$	6	All	$Pamm$	0.81(2)	0.80
(1/4, 1/4,0)	SM2	$(a,0,0,b)$	16	All	$P2_1am$	0.78(3)	0.71

simultaneously a huge shrinkage of the c axis is produced. These structural changes are coupled to a strong electronic localization [20,22] as happens in other A-site ordered perovskites with or without CO [22,36] and A-disordered manganites with CO transitions [45,46]. The structural symmetry of the HT-CO phase is not a direct subgroup of the $Cmmm$ phase and so a first-order transition is expected. This is in agreement with the hysteretic behavior observed in Figs. 6(b) and 6(c), where the two-phase coexistence region is about ∼16 K. Upon heating, the transformation between the two phases is completed in a short range of temperature (see Fig. 6) while the $Cmmm$ phase disappears more gradually on cooling and diffuse scattering assigned to this phase is still visible at 40 K below T_{CO1}. Another feature of this transition is a sharp expansion of the unit cell volume at T_{CO1} as can be seen in Fig. 6(d). This is related to the electron localization and agrees with the virial theorem for a first-order metal-insulator transition [47].

Due to the large changes observed at T_{CO1}, the second structural transition marking the formation of the LT-CO at T_{CO2} goes more unnoticed in Figs. 6(a) and 6(d) but also presents very interesting details. It is a first-order transition as well and shows a hysteresis of about 17 K between the heating and cooling measurements (made at the same rate). As in the previous transition, the $P2_1am$ SG is not a subgroup of $Pnam$ SG taking into account the change of the lattice in the present case. Figure 7 focuses on the changes produced across the transition between the two CO phases (HT-CO and LT-CO). Curiously, the three axes undergo different evolutions across this transition. In this way, the b axis abruptly reexpands at T_{CO2} while the c axis contracts again. The most striking feature is the delta-shaped anomaly observed in the a axis, reproduced in both heating and cooling runs. Under cooling it is seen as a prominent upturn in the evolution of a, that is suddenly released ≈15 K below and abruptly drops. This notable feature may be related to the formation of a polar phase with the electric dipoles oriented along this axis as expected from the point symmetry of the $P2_1am$ SG. Finally, there is no anomaly in the temperature dependence of the unit cell volume mirroring a compensation between changes produced along the different axes.

Given the importance of the CO formation for the metal-insulator transition of SBMO, we have studied the temperature dependence of the Mn valence in the different phases by means of the BVS method [40]. The results are displayed in Fig. 8. The high temperature phase ($Cmmm$, charge
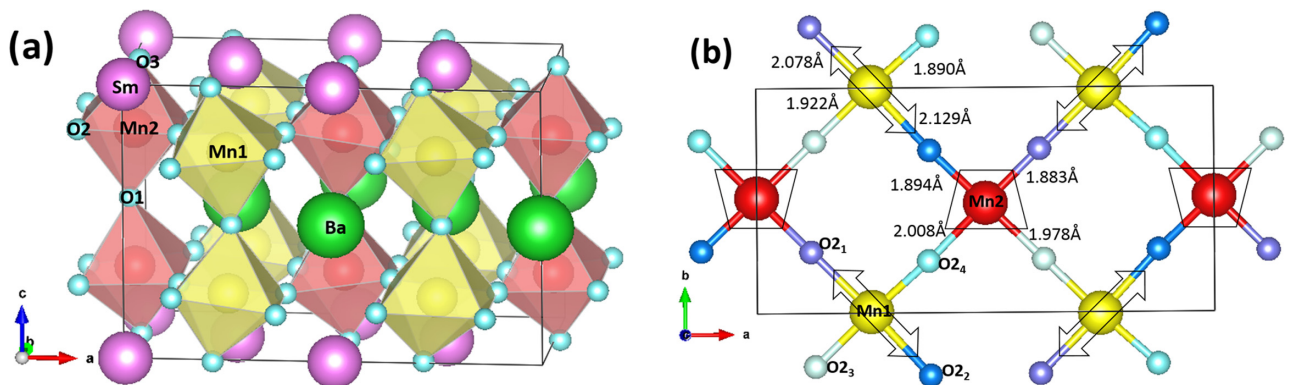
FIG. 5. (a) Crystal structure of SmBaMn$_2$O$_6$ at 100 K corresponding to the LT-CO phase. (b) Top view of the Mn-O layers. The double arrows mark the long Mn-O distances in the Jahn-Teller-like distorted base of the Mn1O$_6$ octahedron while the trapezoids represent the two short and two long Mn-O distances in the base of the Mn2O$_6$ octahedron. Mn1 = Mn$^{3+\delta}$ and Mn2 = Mn$^{4-\delta}$ with $\delta \approx 0.30(6)$.

TABLE VI. Structural parameters of SmBaMn$_2$O$_6$ obtained from the Rietveld analysis at 100 K.

	Atom	Pos.	x	y	Z	B_{iso} (Å^2)
SG: $P2_1am$	Sm1	$2a$	0.0036(9)	0.0024(5)	0	0.39(2)
	Sm2	$2a$	0.2444(9)	0.5000(4)	0	0.39(2)
$a = 11.08815(6)$ Å	Ba1	$2b$	−0.0025(9)	0.0089(7)	$\frac{1}{2}$	0.24(2)
$b = 5.54595(3)$ Å	Ba2	$2b$	0.2452(9)	0.5028(9)	$\frac{1}{2}$	0.24(2)
$c = 7.59275(2)$ Å	Mn1	$4c$	0.2500(8)	0.0055(19)	0.2419(5)	0.18(2)
$V = 466.911(3)$ Å^3	Mn2	$4c$	0.5000(9)	0.4868(9)	0.2483(5)	0.18(2)
	O1$_1$	$2b$	0.2601(13)	−0.024(6)	$\frac{1}{2}$	0.57(5)
$R_p(\%) = 3.8$	O1$_2$	$2b$	0.4899(13)	0.490(6)	$\frac{1}{2}$	0.57(5)
$R_{wp}(\%) = 5.4$	O2$_1$	$4c$	0.1186(16)	0.272(3)	0.7726(17)	0.57(5)
$R_{Bragg}(\%) = 1.95$	O2$_2$	$4c$	0.3782(16)	0.722(3)	0.7847(17)	0.57(5)
$\chi^2 = 6.5$	O2$_3$	$4c$	0.6270(16)	0.237(3)	0.7371(17)	0.57(5)
	O2$_4$	$4c$	0.8758(16)	0.770(3)	0.7945(17)	0.57(5)
	O3$_1$	$2a$	0.214(2)	−0.039(5)	0	0.57(5)
	O3$_2$	$2a$	0.514(2)	0.469(5)	0	0.57(5)

disordered) has a single nonequivalent site for Mn atoms. The BVS calculations yield a mixed valence of $+3.49(1)$, the theoretical one within experimental error. This single valence remains constant down to T_{CO1} where the phase transition splits the Mn site in the *Cmmm* phase into two nonequivalent sites in the *Pnam* cell (Mn$^{3+\delta}$ and Mn$^{4-\delta}$). Just below T_{CO1}, Δq between both sites is very high, approaching the expected value for an ordering of Mn^{3+} and Mn^{4+} cations ($\Delta q \approx 1\,e^-$). Interestingly, Fig. 8 unveils a very appealing unexpected feature of the HT-CO phase: The charge difference continuously decreases with decreasing temperature and stabilizes at ~ 250 K at the value $\Delta q \approx 0.35\,e^-$. Below that temperature and upon further cooling through the second structural transition at T_{CO2}, Δq barely changes and the estimated valence values are split into Mn$^{3+\delta}$ and Mn$^{4-\delta}$ with $\delta = 0.33(1)$ at 100 K (see Table IV). These two last results differ from the ones of Ref. [26], which indicates that the charge segregation was significantly higher in the *Pnam* phase than in the $P2_1am$ phase. It is noteworthy for two reasons. First, only two temperatures were tested in Ref. [26] so the temperature dependence of the charge segregation in each of the phases could be overlooked. Secondly, the values obtained from the BVS calculations strongly depend on the extreme values of the set of bonds lengths. From the data in Tables II and V, it is clear that the distortions observed in both studies are similar and the octahedra environments are quite the same, but the main difference involves the extreme values of Mn-O2 distances, which strongly influence the BVS calculations.

We consider the temperature evolution $\Delta q(T)$ exposed in Fig. 8 to be one of the most appealing findings in SmBaMn$_2$O$_6$. In the following, we want to focus on the exceptional behavior of Δq within the HT-CO phase. For that, it is pertinent to pay attention to the following experimental observations concurrent in our polycrystalline sample: (i) First, Fig. 1 revealed a prominent maximum in the $M(T)$ curve centered at $T_N = 250$ K, separated from the kink that signals the T_{CO2} transition. (ii) Second, the charge disproportionation $\Delta q = 1-2\delta$ between Mn$^{3+\delta}$ and Mn$^{4-\delta}$ octahedra exhibits a huge temperature dependence in the CO-HT state

between 1 and $0.35\,e^-$. Moreover, Fig. 8 clearly reveals that this exceptional continuous reduction of Δq under cooling finishes about $T_N = 250$ K (when Δq reaches $0.4\,e^-$, in a similar way to a lock-in transition). (iii) Third, Fig. 8 proves that below $T_N = 250$ K the charge disproportionation remains unchanged (out of the phase boundary between the two CO phases, near 180 K). (iv) Besides, in Figs. 7(e) and 7(f), respectively, we plot the evolution of a- and b-cell parameters in the T range around the Néel transition. Figure 7(e) reveals a sudden change in the thermal contraction of the a parameter at $T_N = 250$ K (lowering slower). Likewise, a similar but opposite sudden change (lowering faster) of the b parameter can be seen in Fig. 7(f). Notice that these changes at 250 K only occur in the ab plane but no anomaly occurs in the c axis [Fig. 7(c)].

The last observation can be attributed to the appearance below T_N of the presumed CE-type AFM order, in which the spins order parallel to the ab plane, forming FM-coupled zigzag chains [3,11,13,14]. Therefore, the outstanding reduction of Δq as the temperature approaches T_N suggests that the development of FM correlations along the zigzag chains of alternating Mn$^{3+\delta}$-O-Mn$^{4-\delta}$-O atoms entails certain hybridization and electron sharing between Mn$^{3+\delta}$ and Mn$^{4-\delta}$ atoms to produce local double exchange that could trigger the observed reduction in the breathing distortion amplitude (Q_b) of the HT-CO phase.

Finally, it is interesting to compare the LT-CO phase of SBMO with the ground state of similar compounds such as PrBaMn$_2$O$_6$ and NdBaMn$_2$O$_6$. The latter compounds also exhibit a metal-insulator-like transition but there is not CO transition and the low temperature phase is charge disordered with a single site for Mn atoms [36]. In these bigger compounds the MnO$_6$ octahedron has a distortion similar to the Mn$^{4-\delta}$ site in the SBMO compound; i.e., the base of the octahedron exhibits a trapezoidal shape. Thus, it seems to be two types of asymmetric stretching distortions of the basal oxygens competing in RBaMn$_2$O$_6$ (R = Pr, Nd, and Sm) compounds: One belongs to the GM5− irrep and the second to the SM2 one. They both yield two short and
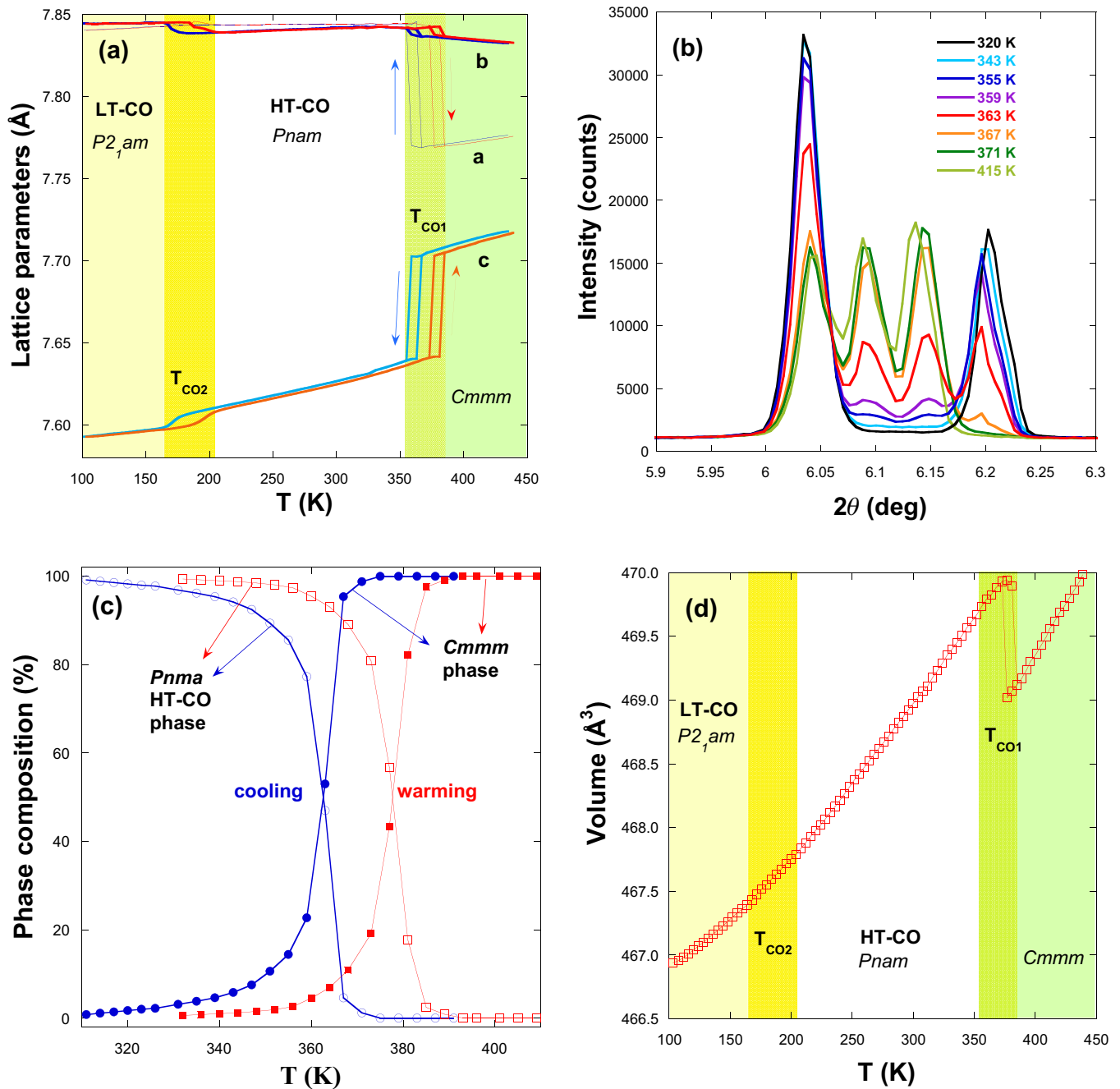
FIG. 6. (a) Temperature dependence of the lattice parameters for SBaMn$_2$O$_6$ in the heating and cooling ramp between 100 and 440 K. The lattice parameters refer to the high temperature phase. (b) Comparison of SRXPD patterns measured at the indicated temperatures heating from 100 K for SmBaMn$_2$O$_6$. (c) Quantification of the high (open symbols) and low (closed symbols) temperature orthorhombic phases. (d) Temperature dependence of the unit cell volume in the heating ramp.

two long Mn-O$_{basal}$ distances. For the bigger Pr^{3+} and Nd^3 cations, the GM5– distortion is large [0.41(3)] [36] and SM2 is absent, which produces short and long distances in opposite edges of the octahedron base (trapezoid shape). The asymmetric stretching distortions occur without charge segregation ($\Delta q = 0$) in the Mn sublattice because breathing distortions such as M4+ or A4+ do not act [36]. In the polar ground state of the smaller Sm^{3+} compound, noticeable

Δq is due to M4+. The GM5– distortion is also present (acting on a different direction). However, one of the SM2 distortions is enhanced, which results in the Jahn-Teller-like distortion in the Mn$^{3+\delta}$ site where the two long distances, as well as the pair of short ones, appear in opposite corners. Coupled with this distortion, the pairs of short and long distances appear in opposite edges for the Mn$^{4-\delta}$ site [Fig. 5(b)].
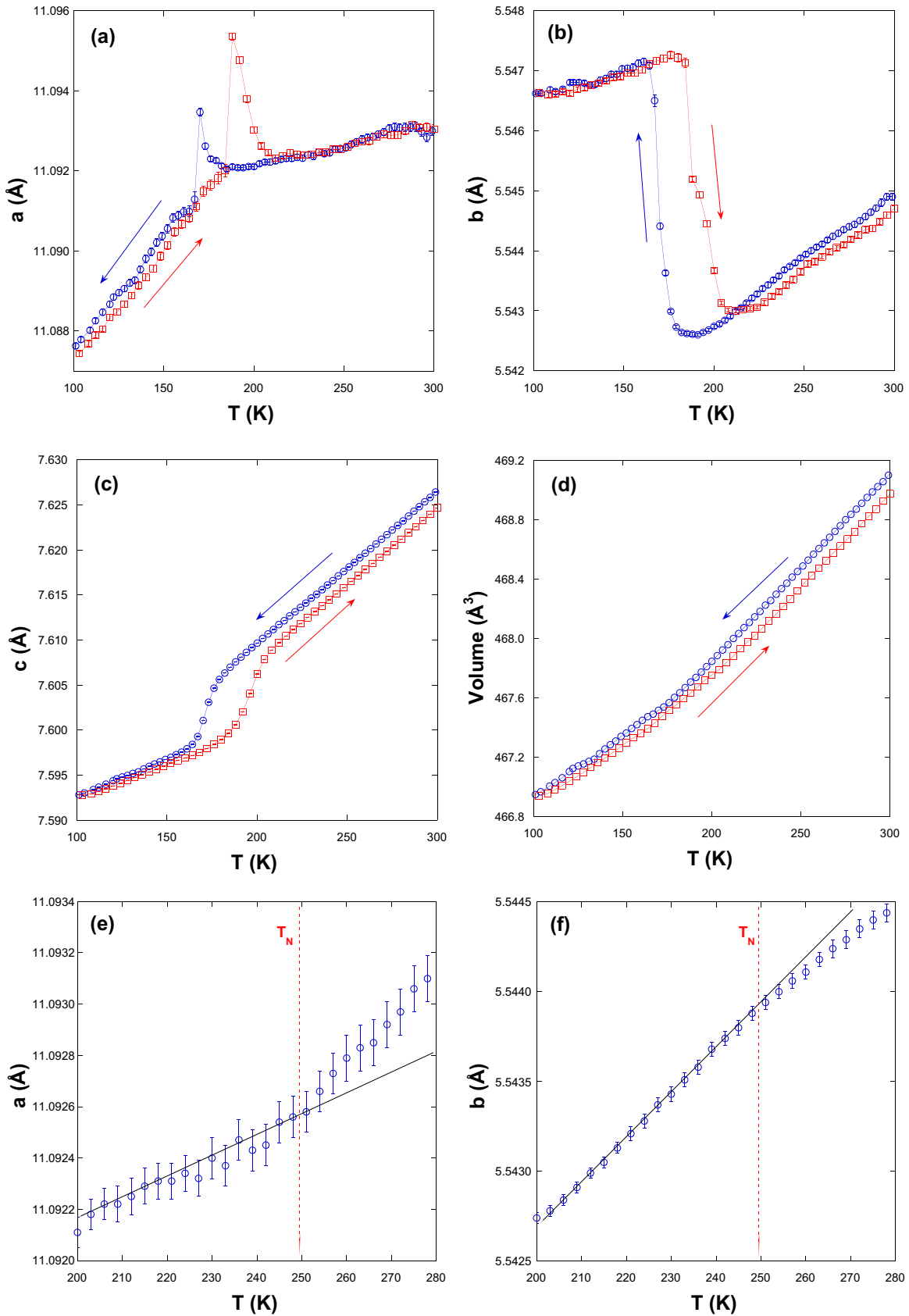
FIG. 7. Temperature dependence in cooling (circles) and heating conditions (squares) for the (a) *a* axis, (b) *b* axis, (c) *c* axis, and (d) unit cell volume of $SmBaMn_2O_6$ between 100 and 300 K. The lattice parameters refer to the LT-CO phase. Detail of the temperature dependence around T_N for the (e) *a* axis and (f) *b* axis in the cooling curve. Dotted line indicates the temperature of the peak maximum observed in the magnetization curve of Fig. 1 while straight lines are guides for the eyes.
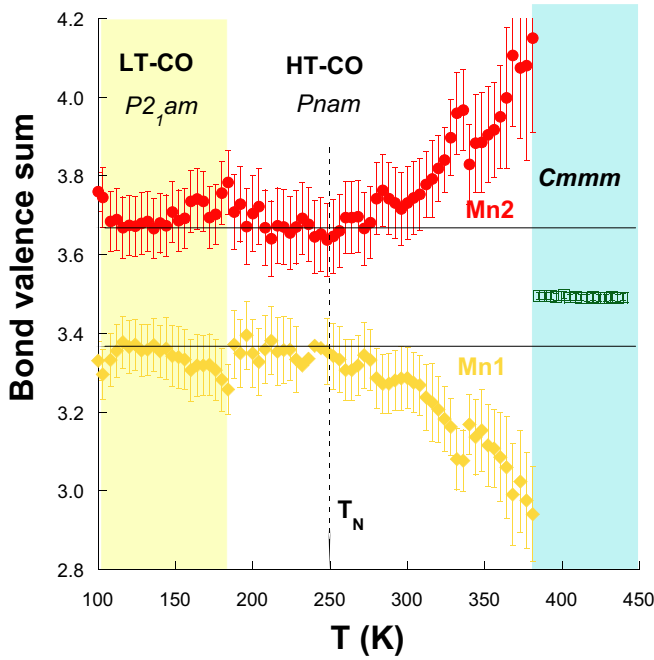
FIG. 8. Temperature dependence of the valences for the different Mn sites in each phase of the SmBaMn$_2$O$_6$ obtained from BVS calculation in the patterns collected in warming conditions from 100 K up to 440 K. The dotted line indicates the value of T_N while the horizontal lines are guides for the eyes.

IV. CONCLUSIONS

In this work, we have investigated the different charge-ordered and magnetic transitions developed by the A-site ordered SBMO perovskite as a function of temperature. We have determined the different distorted structures with respect to the ideal parent tetragonal structure using the symmetry-adapted distortion mode formalism [31]. This method has allowed us to identify the main distortions responsible for the stabilization of each CO and OO phase and its relationship with the emergence of electric polarization. Cooperative tilts of the MnO$_6$ octahedra, which relieve the structural strain produced by the small size of Sm^{3+}, stabilize the high temperature orthorhombic phase with $Cmmm$ SG. In this $Cmmm$ phase, there is only one crystallographic site for the Mn atom that presents a mixed valence state of $+3.49(1)$, the theoretical value within experimental error.

At $T_{CO1} \approx 380$ K, a phase transition occurs mediating by a set of coupled distortions belonging to different irreps and giving rise to the HT-CO phase. Together with the cooperative tilts of MnO$_6$ octahedra, a series of breathing and asymmetric stretching distortions stabilize a checkerboard pattern in the ab plane with two nonequivalent Mn sites. The charge difference between both sites is close to an even mixture of Mn$^{3+\delta}$ and Mn$^{4-\delta}$ with $\delta \approx 1$ at temperatures just below T_{CO1} but it rapidly decreases as the temperature does, stabilizing at a value of $\delta \approx 0.33$ T_N. This result suggests that the develop-

ment of the long-range magnetic ordering requires a decrease in the charge disproportionation that favors electron sharing between Mn$^{3+\delta}$ and Mn$^{4-\delta}$ atoms to yield local double exchange interactions. In addition, the contribution of distortion modes from S2 and Z5– irreps leads to a duplication of the c axis. This involves an exchange between the positions of the two nonequivalent Mn sites every two layers of MnO$_6$ octahedra along this c axis in agreement with the proposed OO scheme AABB [19–23]. However, competition between different distortion modes arising from SM2 and S2 irreps prevents the full formation of a Jahn-Teller-like distortion in the Mn$^{3+\delta}$ site and, thus, OO of e_g $(x^2 - z^2)/(y^2 - z^2)$ orbitals is not completely realized. Instead, the octahedron bases of the two Mn sites are distorted quadrilaterals formed by three short and one long Mn-O bonds in the case of the Mn$^{4-\delta}$ site and the opposite distribution for the Mn$^{3+\delta}$ site. Our study confirms that the SG of the HT-CO phase is nonpolar $Pnam$.

At $T_{CO2} \approx 190$ K, there is a second structural transition with a rearrangement of the structural distortions giving rise to the LT CO phase. The disappearance of modes associated with irreps Z5–, A4+, and S2 leads to the establishment of the checkerboard pattern coherence along the c axis, which is no longer duplicated. The primary distortion modes of the LT-CO phase belong to the M5– irrep associated to cooperative tilts of MnO$_6$ octahedra and the SM2 irrep associated to coupled stretching, twisting, and rotation distortions. Finally, the breathing mode responsible for a checkerboard pattern of MnO$_6$ octahedra with a constant charge disproportionation of about $0.35e^-$ in this phase transforms like a M4+ irrep. Among the individual modes of the SM2 irrep, an asymmetric stretching of the basal oxygens with a Jahn-Teller-like distortion in the Mn$^{3+\delta}$ site is enhanced. Such a distortion could be interpreted as a formal OO phase. However, the same distortion affects the Mn$^{4-\delta}$ site (octahedra sharing corners) producing a trapezoid shape for the base of the Mn$^{4-\delta}$O$_6$ octahedron with alternating orientations along the a axis (see Fig. 5). Therefore, both sites contribute to the anisotropic electronic distribution in the ab plane. Our refinement also confirms that the LT-CO phase is polar, adopting the $P2_1am$ SG. Ferroelectricity is due to distortion modes belonging to the GM5– irrep and the main polar shifts correspond to oxygen atoms and the expected dipoles are located along the a axis.

[1] L. Chen, Z. Xiang, C. Tinsman, Q. Huang, K. G. Reynolds, H. Zhou, and L. Li, Appl. Phys. Lett. **114**, 251904 (2019).

[2] K. Yamauchi, J. Phys. Soc. Jpn. **82**, 043702 (2013).

[3] E. A. Nowadnick, J. He, and C. J. Fennie, Phys. Rev. B **100**, 195129 (2019).

[4] Y. Zhang, H. Zhao, Z. Du, K. Świerczek, and Y. Li, Chem. Mater. **31**, 3784 (2019).

[5] T. Nakajima and Y. Ueda, J. Appl. Phys. **98**, 046108 (2005).

[6] Y. Tokura, Rep. Prog. Phys. **69**, 797 (2006).

[7] Y. Ueda and T. Nakajima, Prog. Solid State Chem. **35**, 397 (2007).

[8] J. M. Rondinelli and C. J. Fennie, Adv. Mater. **24**, 1961 (2012).

[9] N. A. Benedek, J. M. Rondinelli, H. Djana, P. Ghosez, and P. Lightfoot, Dalton Trans. **44**, 10543 (2015).

[10] I. Etxebarría, J. M. Pérez-Mato, and P. Boullay, Ferroelectrics **401**, 17 (2010).

[11] T. Nakajima, H. Kageyama, H. Yoshizawa, and Y. Ueda, J. Phys. Soc. Jpn. **71**, 2843 (2002).

[12] G. Subías, J. García, J. Blasco, and M. G. Proietti, Phys. Rev. B **57**, 748 (1998).

[13] Y. Ueda and T. Nakajima, J. Phys.: Condens. Matter **16**, S573 (2004).

[14] J. Geck, D. Bruns, C. Hess, R. Klingeler, M. v. Zimmermann, S.-W. Cheong, and B. Büchner, Phys. Rev. B **66**, 184407 (2002).

[15] Y. Tokura and N. Nagaosa, Science **288**, 462 (2000).

[16] T. Nakajima, H. Yoshizawa, and Y. Ueda, J. Phys. Soc. Jpn **73**, 2283 (2004).

[17] S. V. Trukhanov, I. O. Troyanchuk, M. Hervieu, H. Szymczak, and K. Bärner, Phys. Rev. B **66**, 184424 (2002).

[18] D. Akahoshi, M. Uchida, Y. Tomioka, T. Arima, Y. Matsui, and Y. Tokura, Phys. Rev. Lett. **90**, 177203 (2003).

[19] M. Uchida, D. Akahoshi, R. Kumai, Y. Tomioka, T. Arima, Y. Tokura, and Y. Matsui, J. Phys. Soc. Jpn. **71**, 2605 (2002).

[20] T. Arima, D. Akahoshi, K. Oikawa, T. Kamiyama, M. Uchida, Y. Matsui, and Y. Tokura, Phys. Rev. B **66**, 140408(R) (2002).

[21] T. Nakajima, H. Kageyama, M. Ichihara, K. Ohoyama, H. Yoshizawa, and Y. Ueda, J. Sol. State Chem. **177**, 987 (2004).

[22] D. Akahoshi, Y. Okimoto, M. Kubota, R. Kumai, T. Arima, Y. Tomioka, and Y. Tokura, Phys. Rev. B **70**, 064418 (2004).

[23] M. García-Fernández, U. Staub, Y. Bodenthin, S. M. Lawrence, A. M. Mulders, C. E. Buckley, S. Weyeneth, E. Pomjakushina, and K. Conder, Phys. Rev. B **77**, 060402(R) (2008).

[24] D. Morikawa, K. Tsuda, Y. Maeda, S. Yamada, and T. Arima, J. Phys. Soc. Jpn. **81**, 093602 (2012).

[25] J. Blasco, J. A. Rodríguez-Velamazán, G. Subías, J. L. García-Muñoz, J. Stankiewicz, and J. García, Acta Mater. **176**, 53 (2019).

[26] H. Sagayama, S. Toyoda, K. Sugimoto, Y. Maeda, S. Yamada, and T. Arima, Phys. Rev. B **90**, 241113(R) (2014).

[27] S. Yamada, Y. Maeda, and T. Arima, J. Phys. Soc. Jpn. **81**, 113711 (2012).

[28] F. Millange, V. Caignaert, B. Domengès, B. Raveau, and E. Suard, Chem. Mater. **10**, 1974 (1998).

[29] J. Blasco, M. C. Sánchez, J. García, J. Stankiewicz, and J. Herrero-Martín, J. Cryst. Growth **310**, 3247 (2008).

[30] J. Rodríguez-Carvajal, Phys. B (Amsterdam, Neth.) **192**, 55 (1992).

[31] J. M. Pérez-Mato, D. Orobengoa, and M. I. Aroyo, Acta Cryst. A **66**, 558 (2010).

[32] B. J. Campbell, H. T. Stokes, D. E. Tanner, and D. M. Hatch, J. Appl. Crystallogr. **39**, 607 (2006).

[33] K. Momma and F. Izumi, J. Appl. Cryst. **44**, 1272 (2011).

[34] F. Fauth, I. Peral, C. Popescu, and M. Knapp, Powder Diffr. **28**, S360 (2013).

[35] M. Aroyo, A. Kirov, C. Capillas, J. Perez-Mato, and H. Wondratschek, Acta Cryst. A **62**, 115 (2006).

[36] J. Blasco, G. Subías, M. L. Sanjuán, J. L. García-Muñoz, F. Fauth, and J. García, Phys. Rev. B **103**, 064105 (2021).

[37] A. M. Glazer, Acta Cryst. A **31**, 756 (1975).

[38] C. J. Howard and H. T. Stokes, Acta Cryst. B **60**, 674 (2004).

[39] See Supplemental Material at http://link.aps.org/supplemental/ 10.1103/PhysRevB.103.214110 for details about x-ray diffraction refinements, schematic representations of atomic displacements, and subgroup details of the distorted structures.

[40] I. D. Brown and D. Altermatt, Acta Cryst. B **41**, 244 (1985).

[41] Y. Shimakawa, Y. Kubo, Y. Nakagawa, S. Goto, T. Kamiyama, H. Asano, and F. Izumi, Phys. Rev. B **61**, 6559 (2000).

[42] R. J. Goff and J. P. Attfield, Phys. Rev. B **70**, 140404(R) (2004).

[43] J. Herrero-Martín, J. García, G. Subías, J. Blasco, and M. Concépcion Sánchez, Phys. Rev. B **70**, 024408 (2004).

[44] S. Lafuerza, J. García, G. Subías, J. Blasco, and P. Glatzel, Phys. Rev. B **93**, 205108 (2016).

[45] R. Kajimoto, H. Yoshizawa, H. Kawano, H. Kuwahara, Y. Tokura, K. Ohoyama, and M. Ohashi, Phys Rev. B **60**, 9506 (1999).

[46] P. G. Radaelli, D. E. Cox, M. Marezio, S.-W. Cheong, P. E. Schiffer, and A. P. Ramirez, Phys. Rev. Lett. **75**, 4488 (1995).

[47] J. B. Goodenough, Aust. J. Phys. **52**, 155 (1999).